Noble Metal Functionalized MoO₃: NiO Nanocomposite for Fabrication of CO₂ Gas Sensor

Authors
M.V. Manasa[1,3], G. Sarala Devi*[1,3], B. Sreedhar[2,3]
[1]Polymer and Functional Materials Division, CSIR-Indian Institute of Chemical Technology (CSIR-IICT), Habsiguda, Hyderabad – 500007
[2]Analytical Division, CSIR-Indian Institute of Chemical Technology (CSIR-IICT), Habsiguda, Hyderabad – 500007
[3]Academy of Scientific and Innovative Research (AcSIR), CSIR-IICT Campus, Habsiguda, Hyderabad-500007
Email: *sarala@csiriict.in, sarala.ipc@gmail.com*; Ph: +91-40-27191532

Abstract
Over the past few years, considerable interest has been focused on semiconducting nanoparticles due to their potential applications in diverse fields including catalysis, magnetic recording media, microelectronics, gas sensors, etc. In our present study, we describe the design, fabrication and gas sensing performance of p-NiO/n-MoO₃ (MN) nanocomposites functionalized by noble metal Au (MNA) in order to develop a reliable sensor for CO₂ gas detection since it is odorless, highly hazardous and toxic green house gas which affects the environment and human health. The formation of the nanocomposite was systematically reviewed and confirmed by X-Ray Fluorescence Spectroscopy (XRF) and X-Ray Diffraction (XRD) patterns. The MN nanocomposite impregnated with noble metal – Au (MNA) showed better efficiency of S=87.86% towards Carbon dioxide (CO₂) gas compared to MN (S=80%) and selectivity towards CO₂ in comparison to other interfering gases with superior stability.
Keywords: *MoO3: NiO: Au nanocomposite; XRF; Particle size Analyzer; XPS; CO₂ Sensor.*

Introduction

In the recent years, need for gas sensors have been ever increasing with the global awareness about the environmental hazards and human safety in the areas such as chemical industries, coal mines, agro farms, etc. for gas leak detection and environmental monitoring[1-3]. Environmental pollution caused by toxic gases, heavy metal ions, organo-phosphorous compounds, industrial and domestic wastes, etc. can directly or indirectly have impact and damage the ecosystem and greatly cause risk to environmental security and human health[4-7]. Hence in the development of gas sensors, nanomaterials play vital role due to their smaller size, high surface-to-volume ratio and reasonably high reactivity with the gas molecules which facilitates excellent sensing performance[8-12]. Studies on various nanomaterials such as ZnO, CuO, SnO, Al_2O_3, Fe_2O_3, SnO_2, In_2O_3, Ga_2O_3, MnO, etc. based gas sensors have been reported for toxic gases like NO_2, NH_3, CH_4, acetone vapours, etc.[13-19]. Z.Y. Can et al reported the gas sensing studies towards CO_2 based on α-Fe_2O_3/CuO exhibiting sensitivity of S=36.8% at 450^oC operating temperature[20]. R. Kocache et al revealed the effective application of nano Ga_2O_3 based sensor towards CO_2 and NH_3 gases with sensitivities 13.4% and 6.8% respectively at 100^oC operating temperature[21]. K. Obata et al have developed MoO_3/V_2O_5 nanocomposite based sensor towards 1000ppm CO_2 gas which exhibited a sensitivity of S=42.1% at 250^oC[22]. Among many synthesis methods like solution combustion, ball milling, micro-emulsion, sol-gel, co-precipitation, hydrothermal, etc., is reported to be an eminent method to synthesize large quantity and homogeneous semiconductor nanomaterials[23-29].

In our present study, we adopted the hydrothermal protocol for synthesis of MoO_3 & NiO nanoparticles since it is feasible, homogeneous and large quantity of the materials can be synthesized. Further Impregnation of noble metal (Au) to the synthesized MoO_3/NiO nanocomposite was done to compel the reaction between the surface of the nanocomposite and CO_2 gas molecules.

Experimental

Synthesis of molybdenum oxide (MoO_3) and nickel oxide (NiO) nanoparticles were carried out via hydrothermal protocol. In a typical synthesis, 1M PEG was dissolved in 100ml D.I. water under continuous magnetic stirring till a clear solution was formed. To this solution, 2M of ammonium molybdate (($NH_4)_6Mo_7O_{24}$) was added and further stirred for 4h to obtain the desired reactant mixture during which the solution changed to grey colour and the solution was transferred into a Teflon coated autoclave, set at 150°C and processed for 4h. After which the reaction vessel was cooled, the obtained precipitate was collected, centrifuged at 4000ppm, oven dried at 80°C/3h and pulverized to obtain fine and homogeneous material which was calcined at 400°C for 2h to eliminate the expected contaminants. Similar procedure was adopted for synthesis of NiO nanoparticles where 3M PEG and 2M nickel acetate (Ni($CH_3COO)_2$) were taken as reactants. 1wt% of nano NiO (optimized wt%) was impregnated in MoO_3 nanoparticles to obtain MoO_3: NiO (MN), further 0.1wt% of Au (optimized wt%) was impregnated into MN to obtain MoO_3: NiO: Au (MNA) nanocomposite. The synthesized nanomaterials were characterized and gas sensing studies were carried out towards CO_2 gas.

Equipment used for Characterization

X-ray powder diffraction data was recorded on Siemens (D5000) diffractometer using Cu Kα radiation (λ = 1.5406 A°) in the range of 2θ = 20–80°. Particle size was recorded by particle size analyzer Horiba SZ100 and the morphological analysis of the samples was done by transmission electron microscopy (TEM) on TEM-TALOS L120C model. UV-Vis DRS was recorded using Perkin Elmer U-2910 UV double beam spectroscopy. X-Ray Fluorescence (XRF) was recorded using OCEAN PUMA 7600D spectrometer. X-Ray Photoelectron Spectroscopy (XPS) was recorded on KRATOS-Axis supra model spectroscope.

Fabrication of the Sensor Element

The substance used for the fabrication of the sensor element was alumina tube of 10 mm length, having two silver electrodes on either side separated by 6 mm, 5 mm external diameter and 3 mm internal diameter. For chemical sensor application, the sensor materials were mixed and ground with deionized water in an agate mortar to form a paste, then the resulting paste was coated on an alumina tube substrate having a pair of silver electrodes on either side followed by drying and calcination at 400°C for 2h. Finally, a Ni–Cr heating wire was inserted into the tube to heat the sensor. The resulting sensor element was subjected to measurements of the electrical resistance in presence and absence of CO_2 gas in air. The operating temperature and concentrations of CO_2 gas were varied in order to establish maximum sensor response. For the resistance measurements the sensor element was placed on a temperature-controlled tungsten coil heater inside the enclosure. A load resistor RL was connected in series with the sensor element Rs. A chromel–alumel thermocouple (TC) was placed on the device to indicate the operating temperature.

The sensitivity (S), defined as the ratio $S=\Delta R/R_a$, where R_a and R_g are the sensor resistance in air and in test gas, respectively, ΔR is the difference between R_a and R_g. The response time is defined as the time required for the variation in conductance to reach 90% of the equilibrium value after which a test gas is injected. The recovery time is the time necessary for the sensor to return to its original conductance state in air[30].

Results and Discussion
X-Ray Diffraction (XRD)

The XRD pattern of the synthesized MoO_3 nanoparticles, MN & MNA nanocomposites is as shown in the figure 1(a-c). The (1 0 1), (4 0 0), (2 1 0), (0 1 1), (2 1 1), (6 0 0), (6 1 0), (020), (1 2 1), (2 2 1) & (8 1 0) planes correspond to MoO_3 which are incoherence with the JCPDS data (no. 897112) with lattice constants a=13.85A^o, b=3.69A^o, c=3.96A^o and lattice angles α=β=γ=90°. The (1 0 4) plane correspond to NiO (JCPDS no. 897390) with lattice constants a=b=2.95A^o, c=7.22A^o and lattice angles α=β=γ=90° whereas the (3 1 1) plane corresponds to Au (JCPDS no. 652870). The crystallite size (D) of the nanomaterials was calculated using Scherrer's formula,

$$D = \frac{K.\lambda}{\beta.Cos\theta} \qquad (1)$$

where K indicates the Scherrer's constant (0.9), λ is the wavelength of X-Ray (1.54A^o), β indicates the full width half maximum of each peak in respective XRD pattern and θ indicates the Bragg's angle of diffraction. The crystallite size of synthesized nano MoO_3 MN & MNA nanocomposites is calculated as 14.26nm, 22.17nm & 17.04nm respectively.
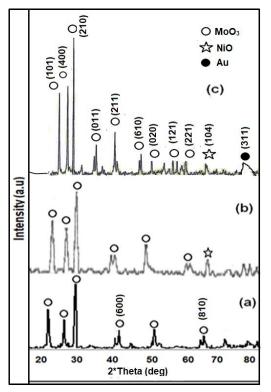

Fig.1 XRD pattern of(a) MoO_3 nanoparticles (b) MN (c) MNA nanocomposites

Particle Size Analysis (PSA)

The particle size distribution of MoO_3 nanoparticles, MN & MNA nanocomposites are as shown in figure 2(a-c). The mean particle size of MoO_3, MN and MNA are observed as 24.8nm, 24.5nm and 22nm respectively, which are incoherence with the respective XRD data. The observed decrease in particle size on addition of noble metal, Au (in present study) is due to the formation of magnetic field during the reaction. This oscillating magnetic field produces electric current through which heat is generated. The heat generation occurs due to eddy current which dissipates into the surrounding from nanoparticles causing thermal ablation resulting in decrease in particle size[13].
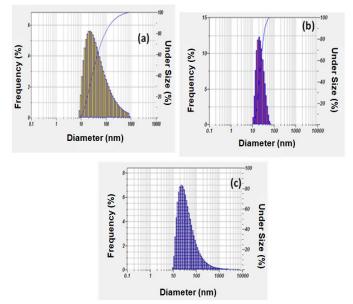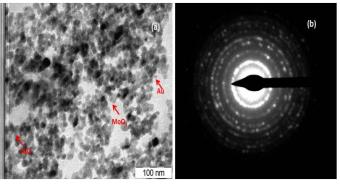

Fig. 2 Particle Size Distribution of (a) MoO_3 nanoparticles (b) MN & (c) MNA nanocomposites

Transmission Electron Microscopy (TEM)

The TEM micrograph and SAED pattern of MNA nanocomposite is shown in figure 3(a,b) which clearly reveals the orthorhombic structure of MoO_3 & black spherical structure of NiO where as the spherical shape particles attached to the surface of MoO_3/NiO may be attributed to Au as seen in 3(a). The selected area electron diffraction (SAED) pattern illustrates spot patterns designating the crystallinity of the material as observed in 3(b).

Fig. 3 (a) TEM micrograph & (b) SAED pattern of MNA nanocomposite

X-Ray Fluorescence Spectroscopy (XRF)

The XRF spectra of MoO_3 nanoparticles, MN & MNA nanocomposites are shown in figure 4(a-c) which confirms the presence of Mo, Ni, O & Au signal in the samples without any impurities.
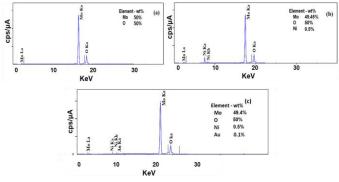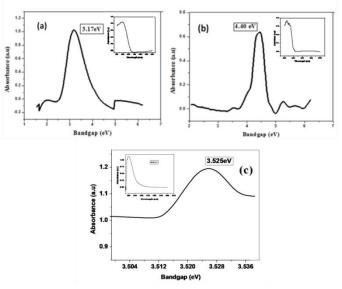

Fig. 4 XRF spectra of (a) MoO_3 nanoparticles (b) MN & (c) MNA nanocomposites

UV-Visible Spectroscopy (UV-VIS)

Figure 5(a-c) gives the Tauc plots and corresponding UV-DRS spectra of MoO_3, MN & MNA nanocomposites. The optical properties of MoO_3 nanoparticles & MoO_3: NiO nanocomposite were measured by UV-Vis diffuse reflectance spectroscopy as shown in the inset of figure 5(a-c) and the bandgap calculated from Tauc plot obtained from UV-Vis DRS data are 3.17eV, 4.40eV & 3.52eV respectively which matches well with the reported semiconductor bandgap. It can be attributed to the intrinsic bandgap absorption of the synthesized nanocomposites since all the samples are direct bandgap materials. The bandgap was estimated from Tauc plot, $(F(R) \, h\upsilon)^{1/2}$ vs. the energy of photon ($h\upsilon$).

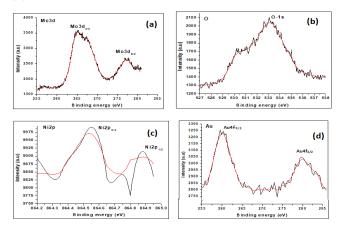$$F(R) = \frac{(1-R)^2}{2R} \qquad (2)$$

Kubel-Ka-Munk function (F(R)) is calculated using the relation shown in equation 2 by analyzing the UV-Vis spectroscopic results where R is the reflectance (%)[30].
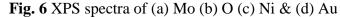

Fig. 5 Tauc plots & UV-DRS spectra of (a) MoO_3 (b) MN & (c) MNA nanocomposites

X-Ray Photoelectron Spectroscopy (XPS)

Figure 6(a-d) shows the XPS spectra of Mo, O, Ni & MNA nanoparticles. Figure 6(a) shows Mo3d core level spectrum which reveals the spin orbit splitting of $Mo3d_{3/2}$ ground state to be 265.19eV while $Mo3d_{5/2}$ excited state is observed at 277.48eV which is attributed to Mo^{+6}. The broadband peak at 533.05eV corresponds to O 1s (figure 6(b)). The two peaks centered at 864.55eV and 864.87eV is assigned to $Ni2P_{3/2}$ and $Ni2P_{1/2}$ respectively as shown in figure 6(c). The Au Spectrum shows two peaks due to spin orbit splitting i.e., $Au4f_{5/2}$ and $Au4f_{3/2}$ at 260.47eV and 279.91eV as seen in figure 6(d).

Fig. 6 XPS spectra of (a) Mo (b) O (c) Ni & (d) Au

Gas Sensing Characteristics

The gas sensing characteristics of MoO_3, MN and MNA nanocomposites were investigated as a function of operating temperature, different concentrations of CO_2 gas and other interfering gases. The changes in the conductivity of the sensor resulting from the interaction with gas molecules are measured as signals.
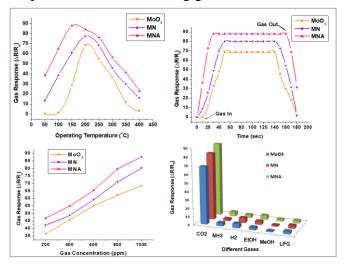
Optimization of the operating temperature is crucial for establishing high sensitivity of the sensor towards the target gas which reveals the sensor response as a function of operating temperature. MoO_3 sensor exhibited low sensitivity to CO_2, In contrast, the observed response of MN sensor has sensitivity of S=80.29% whereas MNA exhibited high sensitivity of S=87.92% followed by a decrease with increase in operating temperature as shown in figure 7(a).

The response–recovery characteristic is equally important to evaluate the overall performance of sensor. The response time (Ts) is the time taken for the sensor to reach 90% of the maximum towards test gas and the recovery time (or decay time (Td)) refers to the time taken by sensor to resume to its original conductivity value. The response and the recovery times were measured towards 1000ppm of CO_2 gas. In case of nano MoO_3 and MN sensor, the response time (Ts) is measured as 50s and recovery time (Td) is 40s respectively whereas for nano MNA sensor, Ts and Td are measured as 30s and 20s respectively as seen in figure 7(b).

Figure 7(c) shows a typical response of the samples MoO_3, MN and MNA sensors as a function of different concentrations of CO_2 gas at their respective operating temperatures. It is observed that the sensitivity increased linearly with the increase in CO_2 gas concentration.

The cross sensitivity was evaluated to determine the selectivity of the sensor towards CO_2 gas. Thus sensitivity studies of the samples MoO_3, MN & MNA were measured at their respective optimum operating temperatures towards 1000ppm of different gases: H_2, ammonia (NH_3), ethanol (ETOH), methanol (MeOH), and LPG. Figure 7(d) represents the resulting data which shows that MNA

is highly sensitivie and selective to CO_2 gas compared to other interfering gases.
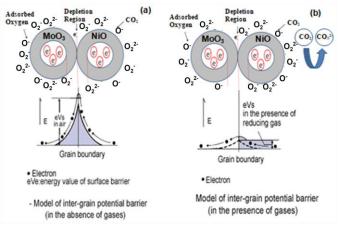

Fig. 7 Gas sensing characteristics of nano MoO_3, MN & MNA – Sensitivity as a function of (a) Operating Temperature (b) Time response (c) Gas concentrations & (d) Different interfering gases

Gas Sensing Mechanism

With reference to our studies we proposed a plausible gas sensing mechanism based on adsorption– desorption mechanism. Oxygen molecules are adsorbed on the MNA surface through two mechanisms: Physisorption and Chemisorption. At low temperature the oxygen molecules are physisorbed on the sensor surface and the bond is weak, leading to a comparatively low response towards CO_2 gas. As the temperature increases, the bond between chemisorbed oxygen ions and MNA surface strengthens. The oxygen species dissociate into more active molecules and atomic ions as follows[15]

$$O_2 \text{ gas} \longleftrightarrow O_2 \text{ ads} + e\text{-} \longleftrightarrow O_2 \text{ ads - } + e\text{- (KT)} \longleftrightarrow O\text{ads - } + e\text{- (KT)} \longleftrightarrow O^{2-} \qquad (3)$$

where O_2 gas is a gaseous oxygen molecule in an ambient atmosphere. The ionization of oxygen molecules occurs due to the capture of electrons from the conduction band of MNA. These oxygen molecules acts as electron acceptors, resulting in a deep electron depletion region with reduces the electron mobility near the surface of oxide as shown in figure 8. This phenomenon enhances the surface potential and work function. When the sensor is exposed to air, O_2 adsorbed on the MoO_3: NiO: Au

(MNA) surface traps electrons from the conduction band of MNA due to strong electro negativity of the oxygen atom, and produces adsorbed oxygen O_2^{n-} (ads) as shown in equation (3). Therefore, the concentration of electrons in the conduction band decreases and the resistance of the material increases. In presence of gas, a chemical redox reaction occurs between CO_2 and adsorbed oxygen, which has relatively strong activation on the surface of MNA nanocomposite. Electrons produced from this redox reaction decrease the resistance of the material thereby increases in the sensitivity. When the MNA sensor is exposed to the air ambient again, the depletion region will be rebuilt by adsorbed oxygen species and the sensor regains its initial resistance.

Fig. 8 Gas Sensing Mechanism (a) In absence and (b) In presence of CO_2 gas

Conclusions

The XRF spectrum of MoO_3: NiO: Au (MNA) nanocomposite shows the presence of Mo, Ni, O & Au signal which confirms the purity of the synthesized sample. The obtained results showed that the MNA nanocomposite sensor showed high sensitivity of 87.8% towards 1000ppm CO_2 gas at a low operating temperature of 150^oC. This proved that the present material (MNA) is highly sensitive and selective to CO_2 gas compared to the other gases demonstrating the potential for developing stable and sensitive gas sensor.

Conflict of Interest

Authors have no conflict of interst

References

1. A. Star, D.W. Steuerman, J.R. Heath, J.F. Stoddart, Dispersion and solubilization of single-walled carbon nanotubes with a hyperbranched polymer, Angew. Chem. Int. Ed., 41, (2002) 2508.
2. Joseph J. Suter, JohnsHopkins, sensors and sensor systems research and Development at ApL with a View Toward the Future, ApL Technical Digest, 26, 4 (2005).
3. Francisco Márquez, Carmen Morant, Nanomaterials for Sensor Applications, Soft Nanoscience Letters, 5, (2015) 1-2.
4. Shao Su, Wenhe Wu, Jimin Gao, Jianxin Lu and Chunhai Fan, Recent Trends in Nanomaterials Applications in Environment, J. Mater. Chem., 22, (2012) 18101.
5. Zhiyu Wang, Srinivasan Madhavi, and Xiong Wen (David) Lou, Ultra long α-MoO_3 Nanobelts: Synthesis and Effect of Binder Choice on their Lithium Storage Properties, J. Phys. Chem. C, 116, (2012) 12508−12513.
6. Sumistha Das, Biswarup Sen, Nitai Debnath, Nanomaterials-based sensors for applications in environmental monitoring, Environmental Science and Pollution Research, 22, 23, (2015) 18333-18344.
7. Joseph J. BelBruno, Nanomaterials in Sensors, Nanomaterials, 3, (2013) 572-573.
8. Liqiang Mai, Fan Yang, Yunlong Zhao, Xu Xu, Lin Xa, Bin Ha, Yanzhu Luo and Hangyu Liu, Molybdenum oxide nanowires: synthesis & properties, Mater. Today, 14, (2011) 7-8.
9. Arnab Ganguly, Raji George, Synthesis, characterization and gas sensitivity of MoO_3 nanoparticles, Bulletin of Materials Science, 30, 2, (2007) 183–185.

10. Arumugam Manivel, Gang-Juan Lee, Chin-Yi Chen, Jing-Heng Chen, Shih-Hsin Ma, Tzzy-Leng Horng, Jerry J. Wu, Synthesis of MoO_3 nanoparticles for azo dye degradation by catalytic ozonation, Mat. Res. Bul., 62, (2015) 184-191.

11. N. Serpone, P. Maruthamuthu, P. Pichat, E. Pelizzetti, H. Hidaka, Exploiting the interparticle electron transfer process in the photocatalysed oxidation of phenol 2-chlorophenol and pentachlorophenol: chemical evidence for electron and hole transfer between coupled semiconductors, Journal of Photochemistry & Photobiology A: Chemical, 85 (1995) 247-255.

12. A. Hernandez, L. Maya, E.S. Mora, E.M. Sanchez, Sol-gel synthesis, characterization and photocatalytic activity of mixed oxide $ZnO-Fe_2O_3$, Journal of Sol-Gel Science and Technology, 42 (2007) 71-78.

13. J. Rabani, Sandwich colloids of zinc oxide and zinc sulfide in aqueous solutions, Journal of Physical Chemistry, 93 (1989) 7707-7713.

14. M.K. Kumar, S. Ramaprabhu, Nano-structured Pt functionalized multiwalled carbon nanotube based hydrogen sensor, Journal of Physical Chemistry B, 110, (2006) 11291-11298.

15. P.S. Prasad Reddy, K. Sreenivasa Reddy, B. Adi Narayana Reddy, M.V. Manasa, G. Sarala Devi and G. Nageswara Rao, Gas Sensing Characteristics of ZnO: Nb_2O_5 Nanocomposite towards Hydrogen Gas, Journal of Advanced Physics, 6, (2017) 418-421.

16. R. Ahuja, L. Fast, O. Eriksson, J.M. Wills, B. Johansson, Elastic and High Pressure Properties of ZnO, Journal of Applied Physics, 83, (1998) 8065-8067.

17. M.D. Driessen, V.H. Grassian, Photooxidation of trichloroethylene on Pt/TiO_2, Journal of Physical Chemistry B, 102, (1998) 1418-1423.

18. A. Fujishima, K. Honda, Electrochemical photolysis of water at a semiconductor electrode, Nature, 238 (1972) 37-38.

19. T. Hisanaga, K. Harada, K. Tanaka, Photocatalytic degradation of organic-hlorine compounds in suspended TiO_2, Journal of Photochemistry & Photobiology A: Chemical, 54 (1990) 113-118.

20. Z.Y. Can, H. Narita, J. Mizusaki, H. Tagawa, State Detection of Carbon Monoxide, Solid State Ionics, 79, (1995) 344-348.

21. R. Kocache, Evaluation and Applications of Gas Sensors, Sensor Review, 14, (1994) 8-12.

22. K. Obata, S. Kumazawa, K. Shimanoe, N. Miura, N. Yamazoe, Potentiometric Sensor based on Nasicon and In_2O_3 for detection of CO2 at room temperature - Modification with foreign substances, Sensors and Actuators B, 76, (2001) 639-643.

23. H. Nanto, H. Sokooshi, T. Kawai, T. Usuda, Zinc oxide thin-film trimethylamine sensor with high sensitivity and excellent selectivity, Journal of Materials Science Letters, 11, (1992) 235-237.

24. E.A. Meulenkamp, Synthesis and growth of ZnO nanoparticles, Journal of Physical Chemistry B, 102, (1998) 5566-5572.

25. G.K. Mor, M.A.Carvalho, O.K. Varghese, M.V. Pishko, C.A. Grimes, A room-temperature TiO_2-nanotube hydrogen sensor able to self-clean photoactively from environmental contamination, Journal of Materials Research, 19, (2004) 628-634.

26. J.H. Yuan, K. Wang, X.H. Xia, Highly ordered platinum-nanotubule arrays for amperometric glucose sensing, Advanced Functional Materials, 15, (2005) 803-809.

27. A.B. Kashyout, M. Soliman, M. El Gamal, M. Fathy, Preparation and characterization of nano particles ZnO films for dye-sensitized solar cells, Materials Chemistry and Physics, 90 (2005) 230-233.

28. S. Anandan, Photocatalytic effects of titania supported nanoporous MCM-41 on

degradation of methylorange in the presence of electron acceptors, Dyes Pigments, 76, (2008) 535-541.

29. J. Kong, M.G. Chapline, H. Dai, Functionalized carbon nanotubes for molecular hydrogen sensors, Advanced Materials, 13 (2001) 1384-1386.

30. Hamoon Hedayat, P. Siva Prasada Reddy, M.V. Manasa, G. Sarala Devi, J.V. Ramana Rao, G. Nageswara Rao, Nanostructure evolution of zinc stannate: A suitable material for liquefied petroleum gas detection, Journal of Alloys and Compounds, 704, (2017) 413-419.